Design, fabrication, and characterization of a D-band bolometric power sensor

Salek, Milan; Celep, Murat; Weimann, Thomas; Stokes, Daniel; Shang, Xiaobang; Phung, Gia Ngoc; Kuhlmann, Karsten; Skinner, James; Wang, Yi

DOI:
10.1109/TIM.2022.3159009

License:
Other (please specify with Rights Statement)

Document Version
Peer reviewed version

Citation for published version (Harvard):
Salek, M, Celep, M, Weimann, T, Stokes, D, Shang, X, Phung, GN, Kuhlmann, K, Skinner, J & Wang, Y 2022, 'Design, fabrication, and characterization of a D-band bolometric power sensor', *IEEE Transactions on Instrumentation and Measurement*, vol. 71, 8002509, pp. 1. https://doi.org/10.1109/TIM.2022.3159009

Design, Fabrication and Characterization of a D-Band Bolometric Power Sensor

Milan Salek, Murat Celep, *Senior Member, IEEE*, Thomas Weimann, Daniel Stokes, *Member, IEEE*, Xiaobang Shang, *Senior Member, IEEE*, Gia Ngoc Phung, *Member, IEEE*, Karsten Kuhlmann, James Skinner, and Yi Wang, *Senior Member, IEEE*

***Abstract*— This paper presents the design, fabrication, and characterization of a D-band (110 – 170 GHz) bolometric power sensor, used for millimetre-wave metrology. This sensor type is new thin-film based sensor which consists of a multilayer-chip embedded in a silicon substrate as a microwave absorber. The sensor demonstrates reasonable performance with a return loss of better than 15 dB across the entire D-band and a rise- and fall-time better than 1.8 ms. The sensor achieves high power linearity between -10 dBm and +8 dBm. Frequency response of the sensor was measured and its flatness changes no more than 20 % across the frequency band. Furthermore, this power sensor has been characterized in the microcalorimeter and an effective efficiency of over 90 % could be achieved. For the first time, the design, fabrication, and characterization of a novel power sensor prototype with excellent performance at D-band are presented.**

***Index Terms*—D-Band, bolometric, power sensor, WR 6.5 waveguide flange, millimeter-wave, metrology, characterization.**

I. Introduction

Power measurement is one of the fundamental measurements in metrology. With the growing interests in millimetre-wave and terahertz applications [1, 2], reliable and accurate RF power measurements are becoming more and more important and indispensable for the emerging applications e.g. 5th and 6th generation mobile networks (5G and 6G), Internet of Things (IoT), Connected and Autonomous Vehicles (CAVs).

One of the requirements for the radio frequency (RF) power measurement is a power sensor and a power-meter. The power sensor plays an important role in RF power measurements which converts high frequency power to a low frequency or DC signal that can be measured using a power meter [3].

However, one of the main challenges is the limited availability of the power sensors for RF power calibration especially when frequencies are increasing. Several types of power sensors are commercially available, such as, thermoelectric, diode-based, thermistors and bolometric sensors. Thermoelectric sensors are based on the working principle of the thermocouple, which generates a DC output voltage, proportional to the input microwave power. Examples of such sensors were reported in [4]-[6]. Diode-based power sensors are based on the rectification properties of the diode. Such sensors were reported in [7, 8]. Bolometric sensors consist of a temperature dependent element such as a thermistor or a thin film. When subjected to a microwave signal, the temperature of its temperature dependent element changes which causes its resistance to change that can be used to determine the amount of microwave power. Several bolometric power sensors have been reported in [9]-[12].

The thermistors power sensors are mostly used by national metrology institutes (NMIs) as reference power standards because they provide high linearity, high reliability and stability, and low measurement uncertainty when used with a primary power measurement system such as microcalorimeter through the DC substitution technique [3]. Coaxial or waveguide thermistors are normally used for RF power calibration at frequencies from a few MHz up to 110 GHz. Though coaxial thermistor mounts are still available up to 18 GHz, waveguide thermistor mounts are out of production for more than two decades. Additionally, it has become impractical to use conventional thermistor bead beyond W-band due to the increasingly restricted space in the waveguide opening. Thus, an alternative approach has to be found. A thin-film bolometric sensor was briefly reported in [11] for D-band (110 - 170 GHz) power standard systems.

With this motivation, this paper presents a new thin-film based D-band bolometric power sensor. It is designed for power

Manuscript received October 20, 2021; revised November 20, 2021; accepted December 20, 2021. Date of publication January 20, 2022; date of current version January 20, 2022. This work was supported by the European Metrology Programme for Innovation and Research (EMPIR) Project 18SIB09 "Traceability for electrical measurements at millimetre-wave and terahertz frequencies for communications and electronics technologies". The EMPIR Programme is co-financed by the participating states and from the European Union's Horizon 2020 Research and Innovation Programme. *(Corresponding author: Milan Salek.)*

M. Salek and Y. Wang are with the Department of Electronic, Electrical and Systems Engineering, University of Birmingham, Birmingham B15 2TT, U.K. (e-mail: m.salek@bham.ac.uk; y.wang.1@bham.ac.uk).

M. Celep, D. Stokes, X. Shang and J. Skinner are with the National Physical Laboratory (NPL), Teddington TW11 0LW, U.K. (e-mail: murat.celep@npl.co.uk; daniel.stokes@npl.co.uk; xiaobang.shang@npl.co.uk; james.skinner@npl.co.uk).

T. Weimann is with Nanostructuring and clean room center infrastructure working group, Physikalisch Technische Bundesanstalt (PTB), D-38116 Braunschweig, Germany. (e-mail: thomas.weimann@ptb.de).

G. N. Phung and K. Kuhlmann are with High-Frequency Base Quantities working group, Physikalisch Technische Bundesanstalt (PTB), D-38116 Braunschweig, Germany. (e-mail: gia.phung@ptb.de; karsten.kuhlmann@ptb.de).

Color versions of one or more of the figures in this paper are available online at http://ieeexplore.ieee.org.

Digital Object Identifier

measuring instruments equipped with standard WR 6.5 waveguide flanges. The multilayer sensor chip relies on a silicon substrate to absorb the microwave power. The power-induced temperature rise is picked up by a platinum thin film layer. Its temperature coefficient of resistance is used to power sensing. The platinum thin film is designed to have an electrical resistance of 200 Ω to be compatible with most existing bridge circuits used in European NMIs.

The paper is organized as follows. Section II describes the design of the D-band power sensor and Section III provides fabrication details of the power sensor. Finally, Section IV presents characterization of the power sensor along with relevant discussion and analysis.

II. POWER SENSOR DESIGN

The core of the power sensor is a multilayer sensor chip of 10.4 mm × 5.65 mm in size. It consists of a silicon substrate which is primarily used as a microwave absorber. The absorbed microwave power raises the temperature of the silicon layer, which heats a thin-film platinum (Pt) line. This temperature change causes the electrical resistance of the Pt line to change, which can be used to determine the amount of microwave power. The internal structure of the power sensor is shown in Fig. 1, with five layers. The chip is sandwiched between two polyimide layers (Layer 1 and 5) for thermal isolation. Polyimide has a loss tangent of 0.031 at 200 GHz and permittivity of 3.24 [13]. Their thickness is ~50 µm. Layer 5 is patterned to allow access to the electrodes.

The second layer is the absorbing layer which is a low-resistivity silicon substrate with a thickness of 200 µm. The silicon has a thermal conductivity of 148 W/K·m and electrical conductivity range of 10 – 100 S/m (1 – 10 Ω·cm) [14]. The third layer is a 1 µm thick silicon dioxide (SiO_2), which electrically isolates the silicon from the platinum thin film on Layer 4. The platinum line is the temperature sensor, with a meander shape. The width, *W*, of this platinum line is 80 µm as shown in Fig. 2.

The electrodes are plated with a thin layer of gold with a thickness of 100 nm, for electrical connection with DC biasing circuit through spring-loaded pin connectors.

For the platinum thin film of chosen thickness of 200 nm and electrical conductivity of 9.524×10^6 S/m at 20 ºC, the sheet resistance (R_s) is calculated as follows. This value is used during the simulations.

$$R_s = \frac{1}{\sigma \cdot t} = 0.525\ \Omega/\text{sq} \quad (1)$$

where σ is the electrical conductivity of the thin film and t is the thickness of the thin film. To obtain 200 Ω for the electrical resistance, the length, *L*, of the meander thin film is optimized to be 30.5 mm.

$$R = \frac{R_S \cdot L}{W} = 200.03\ \Omega \quad (2)$$

Fig. 3 shows simulated response of the power sensor for silicon with electrical conductivity range of 5 – 205 S/m

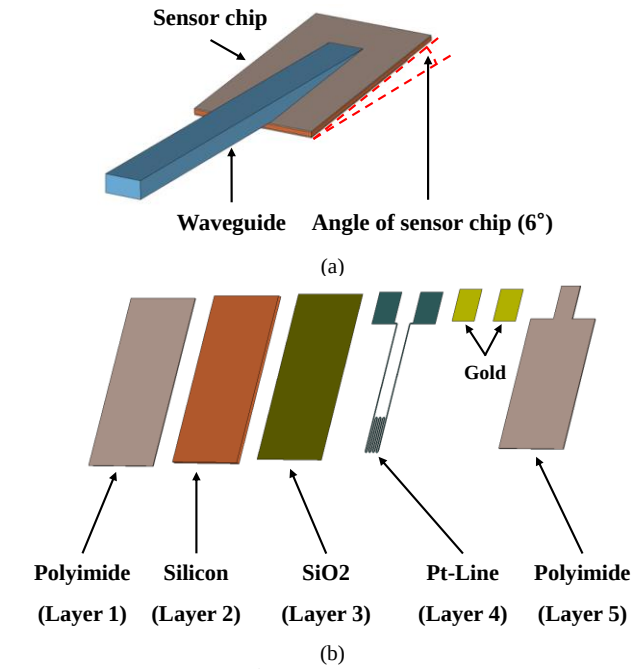

Fig. 1. Internal structure of the D-band power sensor. (a) Air model. (b) Internal layers, shown individually.

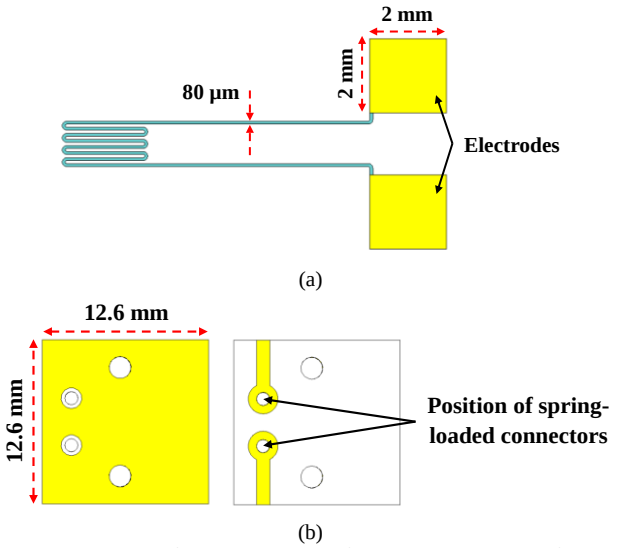

Fig. 2. (a) Structure of the platinum thin film layer. (b) Layout of the PCB which holds both spring-loaded connectors on their position.

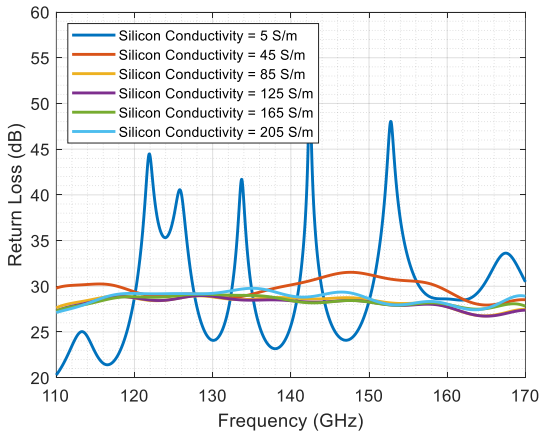

Fig. 3. Effect of changing the electrical conductivity of silicon on the return loss of power sensor.

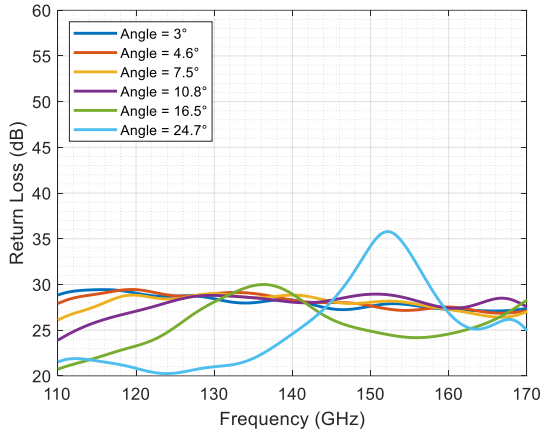

Fig. 4. Effect of changing the sensor chip angle from horizontal on the return loss of power sensor.

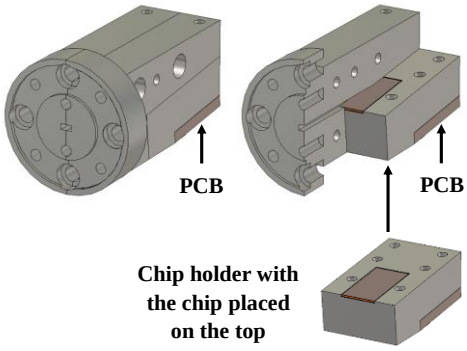

(a) (b)

Fig. 5. External structure of the D-band power sensor. (a) Assembled device. (b) Left half of the flange and waveguide with the chip holder attached. The flange is a standard UG387/U flange with WR 6.5 waveguide.

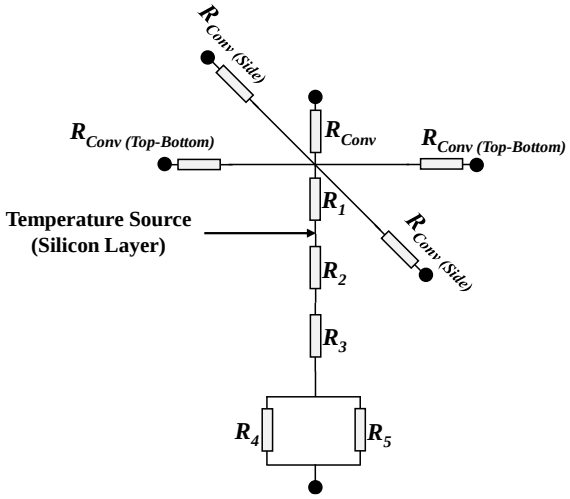

Fig. 6. Equivalent thermal circuit of the D-band power sensor. R_1, R_2, R_3, R_4 and R_5 are the conduction thermal resistance of the first polyimide layer, the silicon dioxide layer, the platinum line, the gold plates, and the patterned polyimide layer, R_{Conv} is the convection thermal resistance in layer direction (inside the waveguide), and $R_{Conv\ (Top\text{-}Bottom)}$ and $R_{Conv\ (Side)}$ are the convection thermal resistances in the direction perpendicular to the layer (chip sides).

(0.4878 –20 Ω·cm). Here, the electromagnetic (em) simulations were performed using CST Studio Suite [15]. In the simulations all the layers are considered as they are denoted in Fig. 1. As it is shown the return loss is near 20 dB across the entire D-band for this conductivity range. So, for the power sensor the closest available silicon with conductivity range of 10 – 100 S/m (1 – 10 Ω·cm) was used.

Based on tolerance analysis in CST [15], the angle of sensor chip from horizontal view (shown in Fig. 1 (a)), is found to be one of the parameters which affects the response of the power sensor. Fig. 4 shows simulated response of the power sensor for different sensor chip angles. Here, the angle was varied from 3° to 24.7°. As it is shown if the angle is within this range, a return loss of above 20 dB can be obtained across the entire D-band. Note that the designed angle from horizontal view is about 6°. Furthermore, the substrate thickness variations of 100 – 600 µm has smaller impact on the response of the power sensor. Based on the simulations and calculations, it is also found that the layer 1 (polyimide layer) only absorbs ~0.12 % of the microwave power, which indicates the effect of the microwave power leakage from layer 1 is negligible.

Fig. 5 shows external structure of the power sensor. It is formed by three blocks. The flange and waveguide are designed in two pieces and cut along the E-plane. The third block is the holder of the sensor chip as shown in Fig. 5 (b) which is bolted onto the waveguide. The flange, waveguide, and the holder are aligned using one horizontal pin on the side and two vertical pins on the back.

The DC contact to the sensor chip is made using a pair of spring-loaded pin connectors. They are held to position by a Printed Circuit Board (PCB) shown in Fig. 2 (b).

The equivalent thermal circuit of the power sensor is shown in Fig. 6, which is used to calculate the conduction and convection thermal resistances of the layered structure. It should be noted that as a rough approximation, the temperature source has been assumed to be the silicon layer which absorbs most of the microwave power dissipation.

Thermal resistance is the ability of a material to resist flow of heat, which can be in three different forms, conduction, convection, and radiation [16]. The conduction thermal resistance can be calculated using

$$R_n = \frac{t}{K \times L \times W} \tag{3}$$

where K is the thermal conductivity of layered material, L is the length of layered material, W is the width of layered material and t is the thickness of layered material.

The convection thermal resistance in the air can be calculated using

$$R_{Conv} = \frac{1}{K_{Air} \times L \times W} \tag{4}$$

where K_{Air} is the convection coefficient of still air which is 5 W/m^2 K and used for calculations and simulations. Finally, the heat radiation can be calculated using

$$P_{Rad} = e \cdot \sigma \cdot A \cdot \left(T^4 - {T_C}^4\right) \tag{5}$$

where e is the emissivity of layered material, σ is the Stephan Boltzmann constant (5.6703×10^{-8} W/m^{2}K^2), A is the

radiating surface area of layered material, T is the temperature of the surface of layered material, and T_C is the temperature of surrounding. For calculations and simulations, an ambient temperature of 23 ºC is used.

Based on calculations using (3), it is found that the conduction thermal resistance of gold plates R_4 has the lowest thermal resistance which was about 4×10^{-5} K/W. However, this layer is thermally isolated by air from one side.

The conduction thermal resistance of platinum thin film layer R_3 is calculated as 2.75×10^{-4} K/W, which is also very low, indicating that the heat flow between the silicon layer and platinum thin film layer is very high. The conduction thermal resistance of silicon dioxide layer R_2 is calculated as 0.013 K/W, which has much lower conduction thermal resistance than the polyimide layer R_1 (4.248 K/W). This should help to transfer the heat from silicon to platinum while ensuring DC insulation.

It is also worth mentioning that the conduction thermal resistance of both polyimide layers (R_1 and R_5 (4.58 K/W)), used for thermal isolation, are high, indicating that the heat flow through them will be very small.

Using (4), the convection thermal resistance in layer direction (inside the waveguide) R_{Conv} is calculated to be 3.4×10^3 K/W, and the convection thermal resistances in perpendicular to layer direction (chip sides) $R_{Conv\ (Top\text{-}Bottom)}$ and $R_{Conv\ (Side)}$ are calculated as 1.77×10^5 K/W and 0.96×10^5 K/W respectively. These are much higher than other thermal resistances, which indicates that the convections heat flow can be neglected.

The analysis above indicates that the heat flow between the silicon layer and platinum is very high, which is what is required, as the maximum heat should be transferred to platinum rather than any other layer. It is also shown that the heat flow between the silicon layer and silicon dioxide is high, which would help the heat to be transferred to platinum.

The heat radiation at the surfaces of the silicon layer was also estimated using (5) to find the amount of heat that could be radiated. However, it is found that the amount of heat that could radiate from the silicon layer is very small and negligible.

III. Power Sensor Fabrication

The waveguide, flange and chip holder are fabricated using CNC (computer numerical control) machining with C109 tellurium copper. Two identical power sensors were fabricated (sensor A and B). One of the sensors is used as a compensation element inside a metal enclosure during characterization measurements. This will be explained further in Section IV. Fig. 7 shows fabricated D-band power sensors.

The chip is fabricated using sputtering and thermal evaporation technique. A 3-inch silicon wafer with 1 µm of silicon dioxide layer on the top was used as a substrate. The wafer has been processed by two lift-off steps using electron-beam lithography technique. In the first step the thin film meander structure and the pads are defined. A 200 nm thick platinum layer with a 2 nm thick adhesion layer of tantalum underneath has been sputtered.

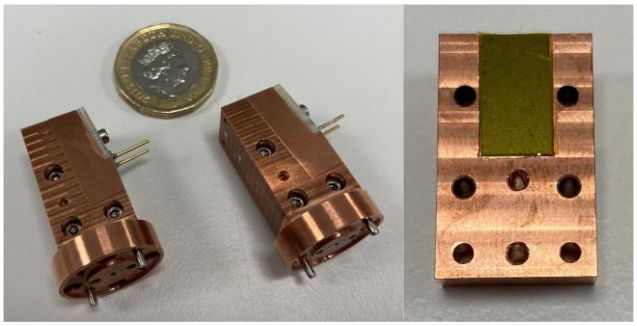

(a) (b)

Fig. 7. Fabricated D-band power sensors. (a) Both power sensors assembled with the PCB and connectors attached. (b) Chip holder with the chip placed on the top.

Fig. 8. Fabricated chip after being cut by the laser.

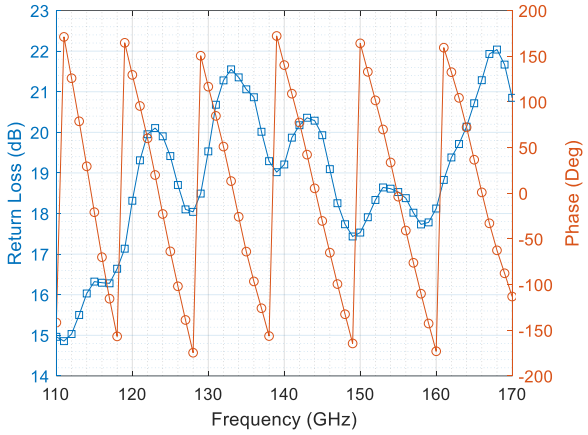

Fig. 9. Measured return loss and phase of sensor A (return loss ( ) and phase ( )).

In the second step the pads are coated with an additional layer of 100 nm thick gold with a 10 nm thick adhesion layer of titanium underneath by thermal evaporation.

The wafer contains 38 chips, which are cut individually by a femtosecond laser cutter with average laser power of 6 W. The laser source was Yuja [17], with a wavelength of 1030 nm, operating at 100 kHz and a beam diameter of 30 µm. Fig. 8 shows one of the chips after being cut. The individual sensors have been wrapped up using Kapton polyimide tape with a thickness of ~50 µm. They are then placed on the chip holders and bolted to the waveguide housings as shown in Fig. 7.

IV. Power Sensor Characterization

To assess the microwave performance of the sensor, voltage reflection coefficient (VRC), short-term time response, long-term time response, linearity and frequency response tests were performed.

A. Voltage Reflection Coefficient

The VRC of sensor A was measured using a D-band waveguide *S*-parameter measurement system. This system consisted of a Keysight PNA-X and VDI VNAX extension modules and was calibrated using a through-reflect-line calibration scheme. The return loss in dB as well as the phase in degree of sensor A are given in Fig. 9 with 1 GHz steps. The return loss of the sensor ranges from 14.9 dB to 22.0 dB with the maximum and minimum return losses measured at 168 GHz and 111 GHz respectively.

B. Short-Term Time Response

Here, the short-term time response of sensor A and B is discussed. A measurement of sensor A's short-term time response to cycling the incident microwave power i.e. changing from power incident on the sensor, denoted as 'on', to not incident, denoted as 'off', and vice versa, was performed to check the rise- and fall-times for the change of sensor resistance. For these measurements, sensor A was located inside a large metal enclosure, as indicated in Fig. 10, which was to isolate the sensor and also cancel short-term ambient temperature fluctuations by keeping the measurement and reference sensor in a stable ambient temperature environment. A second reference sensor (sensor B), which is identical in layout compared to sensor A, was used to measure the ambient temperature effect and was also located within the same metal enclosure. Sensor B was connected to a similar transmission line as sensor A to obtain equivalent thermal mass. A thermal short attached to the input of the transmission lines of the sensors was used to obtain homogeny and similar ambient temperature effects on the two sensors.

A microwave signal generated from a signal generator and a D-band multiplier (illustrated as the signal generator in Fig. 10) was applied to sensor A connected to port 2 of a 10 dB directional coupler. An attenuator and waveguide section were also used in the transmission path. A commercial VDI Erickson PM5 calorimetric type power sensor/meter combination was used to measure the coupled microwave signal at port 3 of the coupler. The output resistances of the sensor elements inside sensor A and B were measured using two Ohm-meters via 4-wire connections. To ensure the thermal equilibrium of the measurement system and the sensors, the setup was kept at a stable room temperature for at least 24-hours prior to the measurement.

The short-term time response measurement was performed at 110 GHz. The microwave power was cycled at 15 and 35 seconds respectively and the outputs of sensor A, sensor B and the power sensor/meter were sampled at an interval of ~1.8 s. Resistance changes of sensor A and B and the coupled microwave power from the directional coupler are shown in Fig. 11.

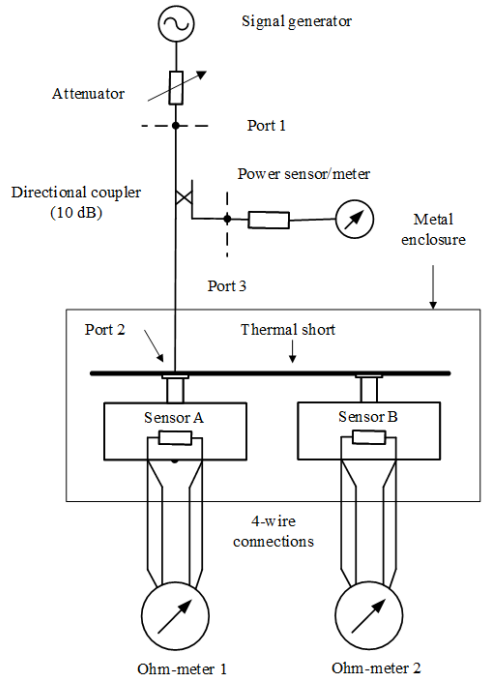

Fig. 10. Schematic diagram for the microwave test setup.

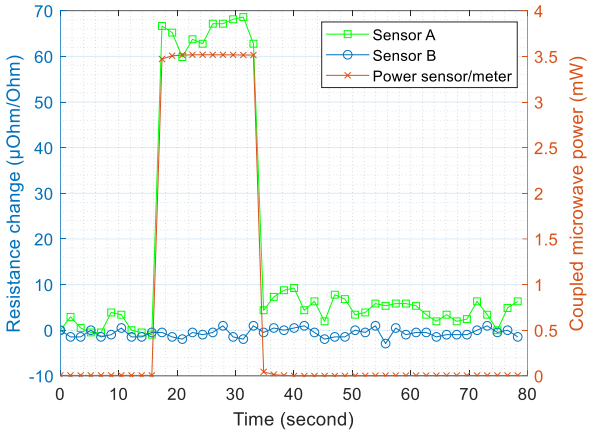

Fig. 11. Sensor A short-term time response to cycled microwave power.

The initial measured resistance values which were used as references for the resistance changes for sensor A and B were 205.50 Ω and 205.60 Ω respectively and the nominal value of the coupled microwave power was 3.5 mW, this coupled power was observed to be stable throughout the measurement. From Fig. 11 the rise- and fall-time for sensor A output resistance can be seen to be less than the sample interval of 1.8 s. The ambient temperature as monitored by sensor B output was observed to be stable throughout the short-term measurement process.

C. Long-Term Time Response

The long-term time response measurement was used to assess the sensor's output drift and was performed using the same measurement setup (Fig. 10), applied microwave frequency and sample intervals as the short-term time response measurement. The difference was an increase in the duration of the power cycles. The power cycle interval was extended to

120 minutes. Sensor A, sensor B and power sensor/meter outputs were taken for two full cycles (i.e. off-on-off-on-off), as shown in Fig. 12 (a). The total measurement time shown in Fig. 12 was 597 minutes.

The results show that the resistance changes due to the microwave power incident on sensor A is not stable over the 120-minutes measurement period and drifts by ~90 μΩ/Ω and a plateau in the middle of the first power-on period can be seen (see Fig. 12 (a)). However, a strong correlation between the sensor A and sensor B output resistance can still be seen. This drift is driven by changes in the systems ambient temperature, with the dominant cause being the dissipated microwave power on sensor A. This indicates a thermal leakage between the sensing element and the wider environment and that sensor A's thermal insulation between the microwave load, flange and housing is insufficient. The average and experimental standard deviations of the resistance change of sensor A and sensor B as well as the power sensor/meter outputs are given in Table I.

The standard deviations for the outputs of sensor A and B are relatively large because of resistance values' drifts in comparison to their corresponding averages whilst the applied microwave power was stable throughout the measurement with its maximum standard deviation lower than 0.04 %.

To eliminate the ambient temperature effects on the observed measurement output for sensor A, the ratio of the sensor A and B resistance was taken and the changes in this ratio over the measurement period are given in Fig. 12 (b). Monitoring this relative change in resistances for the long-term measurement shows a far more stable result, with the ambient temperature effect largely eliminated. The averages and standard deviations for these ratios are also given in Table I. The calculated maximum standard deviation was less than 14 ppm. Furthermore, the thermal leakage from sensor A's microwave load to the housing and consequently to sensor B is evident from the observed rise time, which is estimated at approximately 40 minutes prior to reaching a stable condition. Thermal insulation between microwave load, flange and housing can be improved by increasing the thickness of the polyimide layers or by using a thermal jacket. The time response of the sensor could be improved by reducing the size of the sensor chip.

D. Linearity

A linearity test of sensor A was performed to check the response of the sensor to a range of microwave input power levels. For this test, the attenuator in Fig. 10 was adjusted to obtain different microwave powers at 130 GHz, as indicated by the coupled power sensor/meter and sensor A output resistance. The attenuator was set so that the coupled power sensor/meter indicated a power level of -15 dBm. This was then increased by steps of 5 dB until the maximum power level of the signal generator was reached. For each of these power steps, the same power cycling as for previous measurements was performed. The average of the two off-values for the measured sensors output, each of which were calculated from the average of 150 repeated measurements, were used to minimize the effect of thermal drift. Again, to remove the ambient temperature effect,

TABLE I
AVERAGES AND EXPERIMENTAL STANDARD DEVIATIONS OF THE RESISTANCE CHANGE OF SENSOR A AND SENSOR B. POWER SENSOR/METER OUTPUT AND AVERAGE RESISTANCE RATIONS FOR EACH POWER CYCLE.

Stage	Sensor A μΩ/Ω	Sensor B μΩ/Ω	Power (mW)	Ratio (A/B)
Average				
1st power off	-6.27	-7.38	-0.00207	0.99952248
1st power on	115.4	-8.4	3.49484	0.9996451
2nd power off	1.7	-10.7	-0.00274	0.9995338
2nd power on	133.9	0.2	3.49451	0.9996550
3rd power off	12.8	1.8	-0.00321	0.9995323
Standard deviation				
1st power off	6.17	5.00	0.00058	2.57E-06
1st power on	18.0	11.7	0.00107	1.24E-05
2nd power off	22.9	16.9	0.00071	1.01E-05
2nd power on	22.4	14.2	0.00111	1.13E-05
3rd power off	20.1	9.4	0.00072	1.22E-05

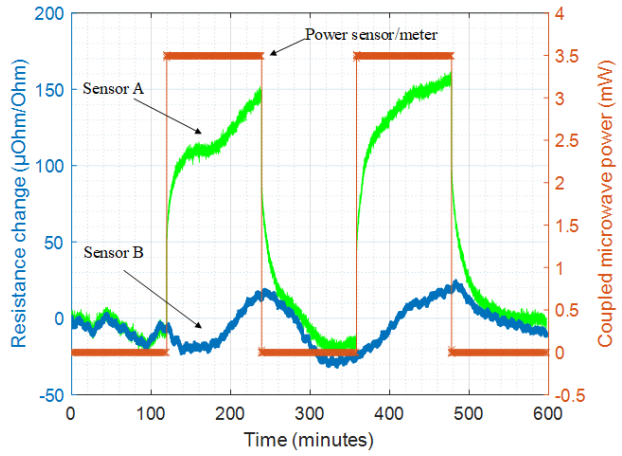

(a)

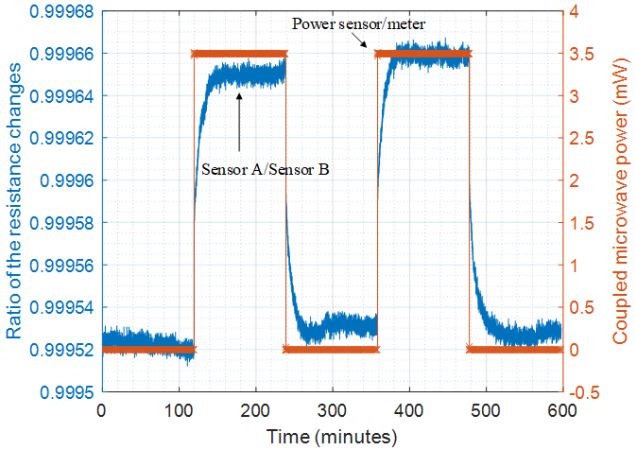

(b)

Fig. 12. Sensor A long-term time response. (a) The resistance changes of sensor A, sensor B and output power on the power sensor/meter. (b) Ratio of the sensor A and sensor B resistance changes and output power on the power sensor/meter.

the ratio to the output resistance changes were used. The power cycle interval was selected as 60 minutes to minimize the temperature leakage effect. The power readings from the power sensor/meter, the resistance change ratios and the linear fitting are depicted in Fig. 13. No corrections were applied to the linearity measurement data as the effective efficiency, which is defined as the ratio of a measured output from the sensor to a

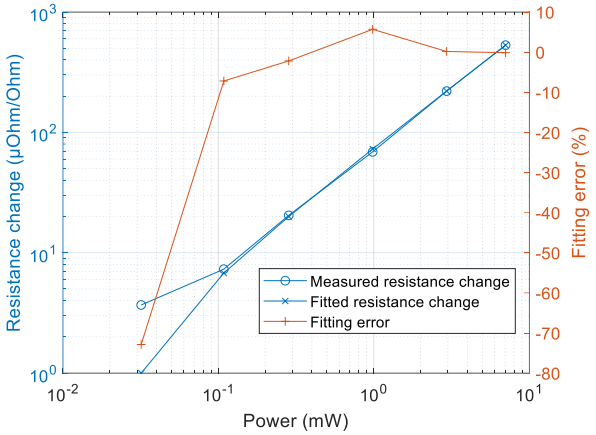

Fig. 13. Sensor A linearity.

known incident microwave power of the power sensor/meter combination [18], measurement system coefficient, sensor A frequency response and VRCs are all assumed to be constants for the measured power range. The fitted line in Fig. 13 was expressed as 75.41210·*P*-1.40497, where *P* is the power in mW measured by the power sensor/meter on port 3. The coefficient of determination, R^2 from 0.03 mW to 7 mW (-15 dBm to 8 dBm) is 0.99989. The difference between the measured and fitted resistance change was also illustrated in Fig. 13, to clearly depict the linearity of the microwave sensor. The maximum observed difference of 73 % corresponds to lowest measured power level of 0.03 mW, being attributed to temperature leakage and the sensitivity of the sensor element to ambient fluctuation because of relatively small signal to noise ratio. For higher power levels, this difference is between -7.2 % and 5.7 %. Therefore, one can conclude that the sensor resistance changes linearly to the applied microwave power from 0.1 mW to 7 mW (-10 dBm to +8 dBm).

E. Frequency Response

The frequency response of sensor A was measured using the setup in Fig. 10. A microwave signal ranging from 110 GHz to 170 GHz in 5 GHz steps was applied to the measurement system and the outputs resistance of the sensor A, sensor B and output power of the power sensor/meter were measured. The frequency response was defined as a ratio of the change in the sensor A output resistance due to the applied microwave power at each frequency. The power sensor/meter was used as a calibrated reference and its effective efficiency was previously measured using a calorimeter technique including the sensors described in this manuscript [19].

The measured power incident on the power sensor/meter (P_A) was translated to the equivalent incident power on the sensor A input using a system coefficient (Sc), which was calculated using the measurement system parameters and given as:

$$Sc = \frac{|S_{31}|^2}{|S_{21}|^2} \frac{1-|\Gamma_{SA}|^2}{1-|\Gamma_{STD}|^2} \frac{|1-\Gamma_2\,\Gamma_{STD}|^2}{|1-\Gamma_3\,\Gamma_{SA}|^2} \quad (6)$$

where, Γ_{SA} and Γ_{STD} are the VRC's of sensor A and the power sensor/meter combination connected to the ports 2 and 3 respectively. Γ_2 and Γ_3 are the VRC's of the port 2 and port 3 of the measurement system. S_{21} and S_{31} are voltage transmission coefficients from port 1 to port 2 and port 3 respectively. The incident microwave power on sensor A was calculated using the system coefficient, effective efficiency of the power sensor/meter combination (EE) and output power

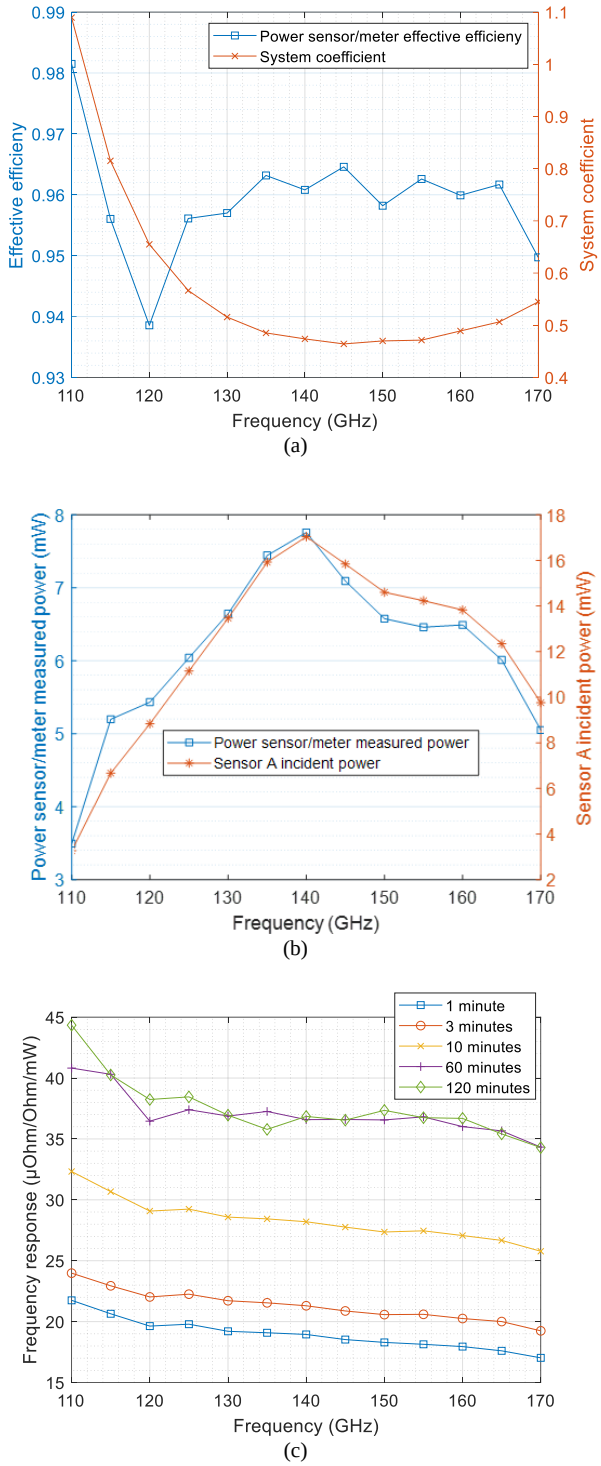

Fig. 14. Sensor A frequency response (T_D). (a) Power sensor/meter effective efficiency and measurement system coefficient. (b) Measured microwave power from the power sensor/meter output and calculated sensor A incident power. (c) Sensor A frequency response after 1-, 3-, 10-, 60- and 120-minutes waiting time.

(P_A) of the power sensor/meter as,

$$P_D = \frac{P_A}{EE\ Sc} \tag{7}$$

Finally, the corrected frequency dependent response of the sensor was determined using the same resistance ratio method as previously described using the outputs from both sensor A and B as,

$$T_D = \frac{\Delta R}{P_D} \tag{8}$$

where, ΔR is the ratio of the output resistance changes of the sensor A and B. In practice, the incident microwave power on sensor A (P_D) can be calculated with re-arranged (8) using known T_D and ΔR.

The system parameters in (6) were measured using the D-band *S*-parameter measurement system described in Section IV.A. The system coefficient and effective efficiency, given in Fig. 14 (a), vary from 0.46 to 1.1 and 0.93 to 0.99 respectively across the frequency band.

As previously discussed, the system has a non-zero thermal settling time due to leakage between components, the sensor A frequency response was measured over five different time intervals 1, 3, 10, 60 and 120 minutes. To minimize this temperature effect, the sensor outputs were measured over 50 repeated power cycles and the sensor output for microwave-off was calculated as the average of the two off stages before and after on. Furthermore, the sensor output was also normalized to the sensor B resistance to obtain ΔR.

The output power of the power sensor/meter combination and incident sensor A power which was calculated using (8) are illustrated in Fig. 14 (b) as measured over a 3-minutes time interval. The measured power on the power sensor/meter and calculated incident power on the sensor A are between 3 to 8 mW and 3 to 17 mW respectively.

The frequency response for five different time intervals is depicted in Fig. 14 (c). The frequency response for sensor A can be seen to change with each time intervals up until the 60- and 120-minutes measurements. This agrees with the rise time as shown in the long-term time response measurement. The result obtained after 120 minutes is very similar to that obtained after 60 minutes. On the other hand, the frequency response of the sensor is relatively linearly changing in the frequency range and maximum deviation is around 20 % at 110 GHz for all time intervals.

V. Conclusion

This paper has presented the design, fabrication, and characterization of a D-band bolometric power sensor. The power sensor presented in the paper consists of a multilayer chip which is housed in a WR 6.5 waveguide flange. The chip uses a silicon layer as a microwave absorber. The absorbed microwave power results in silicon temperature rise, which heats a platinum thin film. This causes the thin film resistance to be changed which can be used to measure the microwave power. The characterized results showed that the sensor has an excellent matching across the entire D-band with a return loss of better than 15 dB and its slope is relatively flat. The sensor performed well within a stable environment with the sensor resistance changed linearly to the applied microwave power from 0.01 mW to 7 mW. However, based on the long-term time response, it is found that there is a thermal leakage between the sensor chip and the wider environment due to the insufficient thermal insulation between the microwave load, flange, and housing. The long-term (> 40 minutes) frequency response of the sensor from 110 GHz to 170 GHz was measured highly linear at around 37 μΩ/Ω/mW.

The sensor is suitable for micro-calorimeter applications for primary level microwave power definition [19] and can be used for microwave power measurements within stable environmental conditions by considering thermal equilibrium and the frequency response.

Acknowledgment

Authors would like to thank Professor Michael Lancaster (University of Birmingham), Dr Aydin Sabouri (University of Birmingham; currently with University College London), and Rolf Judaschke and Jürgen Rühaak (PTB, Germany) for their advice.

References

[1] A. D. Panagopoulos, P.-D. M. Arapoglou, and P. G. Cottis, "Satellite Communications At KU, KA, And V Bands: Propagation Impairments And Mitigation Techniques," *IEEE Communications Surveys & Tutorials*, vol. 6, no. 3, pp. 2–14, 2004.

[2] C. Dehos, J. L. González, A. D. Domenico, D. Kténas, and L. Dussopt, "Millimeter-Wave Access and Backhauling: The Solution to the Exponential Data Traffic Increase in 5G Mobile Communications Systems?," *IEEE Communications Magazine*, vol. 52, no. 9, pp. 88–95, 2014.

[3] X. Cui, Y. S. Meng, Y. Shan, and Y. Li, "Microwave Power Measurements: Standards and Transfer Techniques," *New Trends and Developments in Metrology*, 2016.

[4] V. Milanovic, M. Gaitan, E. Bowen, N. Tea, and M. Zaghloul, "Thermoelectric Power Sensor for Microwave Applications by Commercial CMOS Fabrication," *IEEE Electron Device Letters*, vol. 18, no. 9, pp. 450–452, 1997.

[5] Z. Zhang, X. Liao, and X. Wang, "Research on Thermocouple Distribution for Microwave Power Sensors Based on GaAs MMIC Process," *IEEE Sensors Journal*, vol. 15, no. 8, pp. 4178–4179, 2015.

[6] S. Kodato, T. Wakabayashi, Q. Zhuang, and S. Uchida, "New Structure for DC-60 GHz Thermal Power Sensor," *1996 IEEE MTT-S International Microwave Symposium Digest*, pp. 871-874, vol.2, 1996.

[7] K. Xu, Y. Zhang, L. Xie, and Y. Fan, "A Broad W-band Detector Utilizing Zero-bias Direct Detection Circuitry," *2011 International Conference on Computational Problem-Solving (ICCP)*, pp. 190-194, 2011.

[8] L. A. Tejedor-Alvarez, J. I. Alonso, and J. Gonzalez-Martin, "An Ultrabroadband Microstrip Detector up to 40 GHz," *2008 14th Conference on Microwave Techniques*, pp. 1-4, 2008.

[9] K. Sakurai and T. Nemoto, "A Thin-Film Bolometer Unit," *IEEE Trans. Instr. Meas.*, vol. 16, no. 3, pp. 206–211, 1967.

[10] L. Brunetti, "Thin-film bolometer for high-frequency metrology," *Sensors and Actuators A: Physical*, vol. 32, no. 1-3, pp. 423–427, 1992.

[11] X. Wang, Q. Zhong, J. Li, W. Yuan, Y. Li, and X. Cui, "WR-06 Power Standard Devices," *2018 Conference on Precision Electromagnetic Measurements (CPEM 2018)*, pp. 1-2, 2018.

[12] D. D. Dinh and M. J. Lancaster, "Microwave Power Sensors With Integrated Filtering Function for Transfer Power Standards," IEEE Microw. Wireless Compon. Lett., vol. 30, no. 3, pp. 308-311, 2020.

[13] Fujifilmusa.com. 2020. [online] Available: https://www.fujifilmusa.com/shared/bin/Durimide%207000_US12.pdf. [Accessed: 28-May-2020].

[14] *Silicon, Quartz, Glass and Fused Silica Wafer*. [Online]. Available: https ://www.microchemicals.com/products/wafers/wafer_si_sio2_3_inch_en.html. [Accessed: 28-May-2020].
[15] Computer Simulated Technology (CST). (2019). Microwave Studio. [Online]. Available: http//www.cst.com/.
[16] F. P. Incropera, D. P. DeWitt, T. L. Bergman, and A. S. Lavine, *Principles of heat and mass transfer*. Hoboken (New Jersey): J. Wiley & Sons, 2017.
[17] Yuja. (2020). [Online]. Available: https://amplitude-laser.com/products/femtosecond-lasers/yuja/.
[18] M. Celep and D. Stokes, "Characterization of a Thermal Isolation Section of a Waveguide Microcalorimeter," *IEEE Trans. Instr. Meas.*, vol. 70, pp. 1-7, 2021, Art no. 1008007, doi: 10.1109/TIM.2021.3084306.
[19] M. Celep, M. Salek, D. Stokes, J. Skinner and Y. Wang, "Power Sensor Characterization from 110 GHz to 170 GHz using a Waveguide Calorimeter," *IEEE Trans. Instr. Meas.*, early access, Jan. 20, 2022. Doi: 10.1109/TIM.2022.3144209.